CrossMark

Investigation on spinel MnCo$_2$O$_4$ electrode material prepared via controlled and uncontrolled synthesis route for supercapacitor application

R. Tholkappiyan[1] · A. Nirmalesh Naveen[1] · S. Sumithra[1] · K. Vishista[1]

Abstract To analyze the impact of preparation routes on the electrochemical behavior of nanoparticles, manganese cobaltite (MnCo$_2$O$_4$) has been synthesized by combustion (MnC-C) and hydrothermal route (MnC-H). The structural properties of synthesized nanoparticles were characterized by X-ray diffractometer studies which confirm the formation of cubic spinel phase with average crystallite size of 26 nm for combustion route prepared and 24 nm for hydrothermal route. The FT-IR spectrum shows two strong bands observed at 651 and 559 cm^{-1} that are characteristic to stretching vibrations of tetrahedral and octahedral sites of spinel MnCo$_2$O$_4$ compounds. Elemental analysis, oxidation state, and chemical composition of these nanoparticles were examined using X-ray photoelectron spectroscopy. The morphology of synthesized nanoparticles was analyzed by SEM images. Loosely packed flake-like morphology was observed for MnC-H and typical spongy network structure with voids or pores was seen for MnC-C samples. BET analysis reveals the presence of mesopores and micropores in the prepared compounds. Influence of preparation route on capacitor behavior was evaluated by performing electrochemical characterizations such as cyclic voltammetry, chronopotentiometry, and AC impedance analysis. MnC-H exhibits a higher specific capacitance of 671 F g^{-1} at 5 mV s^{-1} scan rate compared to 510 F g^{-1} exhibited by MnC-C electrode material. Excellent capacitance retention of 92 % was demonstrated by MnC-H over 1000 continuous cycling. Results indicate that MnCo$_2$O$_4$ prepared via controlled synthesis conditions (hydrothermal) shows better performance than combustion prepared.

Introduction

In recent years, research on electrode materials for supercapacitor applications has gained greater interest. Supercapacitor or electrochemical capacitor is an electrochemical energy storage device superior to its conventional dielectric counter parts in many aspects [1, 2]. Owing to their fast charge/discharge characteristics, flexibility and long lifespan, they have attracted wide applications such as auxiliary power source in hybrid vehicles, portable mobile devices, ignition systems, micro-electronics, rockets etc., [3, 4]. Based on the different operation mechanisms, the supercapacitors can be classified into two different categories: (1) double-layer capacitors, which are based on the non-faradic charge separation at the electrode/electrolyte interface and (2) pseudocapacitors, which are based on the faradic redox reaction of electroactive materials [5]. Recently, with the purpose of achieving high energy density supercapacitors, great efforts have been devoted to search for excellent pseudocapacitive materials. Amorphous hydrated ruthenium oxide has been demonstrated to be an excellent pseudocapacitor material, which exhibits a high conductivity, good electrochemical stability, and a large specific capacitance (SC) of 720–760 F g^{-1}. However, high cost and toxicity of the ruthenium oxide greatly limit its commercial applications. Thus, other less expensive and less toxic transition metal oxides such as MnO$_2$, Co$_3$O$_4$, MoO, V$_2$O$_5$, NiO, and Fe$_2$O$_3$ were explored. Cobalt oxide and manganese oxide were extensively studied for their superior capacitive behavior. It is reported that mixed oxide composites exhibit

✉ K. Vishista
raovishista@gmail.com

[1] Department of Physics, College of Engineering, Guindy, Anna University, Chennai 600025, India

superior capacitive performance to single transition metal oxides [6–10].

Complex oxides (containing two or more types of cations) with spinel structure under controlled size and shape are of intense interests for both fundamental science and technological applications because of their chemical and physical properties [11–13]. Complex oxides such as $MnCo_2O_4$ [14, 15], $ZnMn_2O_4$ [16], $NiCo_2O_4$ [17], $NiFe_2O_4$ [18], and $ZnCo_2O_4$ [19] etc., have been investigated as electrode materials for supercapacitors because of their excellent electrochemical performances. Among them, manganese-based oxide spinels are useful in many application fields (transport, telecommunication, medicine, and energy) due to their element abundance, low cost, and toxicity and electrical characteristics [14, 15]. There are only few researcher works on $MnCo_2O_4$ for supercapacitor applications. Li et al. have synthesized one-dimension $MnCo_2O_4$ nanowire arrays on nickel foam by facile hydrothermal method with a SC of 349.8 F g^{-1} at 1 A g^{-1} and 328.9 F g^{-1} at 20 A g^{-1} [14]. A thin film binder-free Co–Mn composite oxide ($MnCo_2O_4$) electrode was synthesized through electroless-electrolytic (EE) techniques by Jamie Gomez et al. with a SC of 832 F g^{-1} at a scan rate of 20 mV g^{-1} [15]. Various concentrations (5–20 %) of manganese ions-doped cobalt spinel oxide were synthesized by A N Naveen and S Selladurai via co-precipitation method with 20 % Mn which exhibits the highest SC of 440 F g^{-1} [20]. Prasad and Miura reported that the addition of Co oxide can improve the SC of Mn oxide electrodes synthesized by potentiodynamic methods from 482 to 498 F g^{-1} at 10 mVs^{-1} [21]. However, most of the researches of $MnCo_2O_4$ focus on thin films materials or nanopowders; there still exist several drawbacks, such as cation distribution and low utilization of active materials.

There has been different cation distributions proposed in the literature for the sample $MnCo_2O_4$. The cation distribution in spinels is directly influenced by the synthesis condition and thermal treatment. For instance, the quenching of a sample at room temperature can fix a distribution that is usually out of its thermodynamic equilibrium when slowly cooled [22]. Various cation distributions have been proposed for $MnCo_2O_4$; previously, Gautier et al. have suggested $Co^{2+}[Mn^{2+}_{0.35}Co^{3+}Mn^{3+}_{0.29}Mn^{4+}_{0.36}]O_4$, whereas Blasse have shown $Co^{2+}[Co^{2+}Mn^{4+}]O_4$, Kolomiets et al. $Co^{3+}[Mn^{2+}Co^{3+}]O_4$, Wickman and Croft $Co^{2+}[Co^{3+}Mn^{3+}]O_4$, and Gobanov $Co^{2+}[Co^{2+}Mn^{4+}]O_4$ [23–27].

From these observations, it can be understood that the preparation conditions of this system have potential impact on the electrode parameters such as phase, morphology, cation distribution, and electrical properties thereby controlling the supercapacitive behavior. Hence, we made an attempt to prepare $MnCo_2O_4$ spinel compound via two different methods (combustion and hydrothermal) and studied the influence of preparation conditions on the materials structural, chemical, and electrochemical properties. Both combustion and hydrothermal synthesis methods have their unique advantages affecting the physiochemical properties of the prepared nanomaterials. Combustion synthesis or self-propagating high temperature synthesis is an effective, low-cost method for the preparation of nanomaterials, and industrialization of combustion synthesis has been realized. One of the advantages of combustion synthesis is the rapid decomposition of complexant at low temperature with simultaneous evolution of large amount of gases. Low decomposition temperature and evolution of gases result in a high degree of nucleation and slow growth rate of the particles favoring the formation of nearly mono-dispersed nanoparticles [28, 29]. Hydrothermal synthesis is generally defined as crystal synthesis or crystal growth under high temperature and high pressure water conditions from substances which are insoluble in ordinary temperature and pressure (<100 °C, <1 atm). The solvent properties for many compounds, such as dielectric constant and solubility, change dramatically under supercritical conditions. The particle size of metal oxide depends on the hydrolysis rate and solubility of the metal oxide [30]. Several controlled uniform nanostructured materials have been previously developed using hydrothermal synthesis method [31–34]. Li et al. have synthesized one-dimension $MnCo_2O_4$ nanowire arrays on nickel foam by facile hydrothermal method with a SC of 349.8 F g^{-1} at 1 A g^{-1} and 328.9 F g^{-1} at 20 A g^{-1} [14].

From this discussion, it would be realized that combustion is the process which occurs through self-ignition of the fuel where the rate and phase formation of the product becomes completely uncontrolled. Conversely, in hydrothermal synthesis, one has precise control over the hydrolysis, nucleation, and growth of nanoparticles by controlling reaction temperature and pressure. It would be worthwhile to study the impact of these two distinct growth mechanisms on the supercapacitor behavior of manganese cobaltite system.

Experimental

Synthesis of manganese cobaltite by combustion route

A stoichiometric ratio of manganese nitrate ($Mn(NO_3)_2$ ·4H$_2$O, Alfa Aesar 98 %) and cobalt nitrate ($Co(NO_3)_2$ ·6H$_2$O, Alfa Aesar 98 %) was taken in a beaker containing water and mixed magnetically for 15 min. Then 5 ml of conc. nitric acid (HNO_3) was added to the mixture to obtain a homogeneous clear solution. The appropriate amount of

glycine (fuel) ($C_2H_5NO_2$, Qualigens 98.5 %) was then added to the above solution and the mixture was stirred until complete dissolution occurred. The mixture in the form of gel was heated at temperature of about 100 °C under constant stirring to remove inherent water present in the solution. The dried gel was transferred to a hot plate and heated at 150 °C until self-ignited. Continuous heating leads to the auto-ignition of dried gel with the evolution of large quantities of gases. Ash obtained from the combustion synthesis was amorphous and it was subjected to calcination at 400 °C for 4 h. Final product was grounded thoroughly and labeled as MnC-C.

Synthesis of manganese cobaltite by hydrothermal route

In a typical procedure, one T-spoon of ethylene glycol dissolved in 10 ml of distilled water was added drop wise into a clean glass beaker containing 1:2 molar ratio of manganese nitrate and cobalt nitrate and stirred continuously at room temperature for 2 h. The resulting solution was added with required amount of sodium hydroxide (NaOH, Qualigens 98 %) with heat treated at 40 °C and stirred for 10 min. The resultant solution was transferred to an autoclave and kept in hot air oven at 120 °C for 36 h. The resulting solution was allowed to cool to room temperature and washed with water for several times followed by ethanol and acetone to remove the excess of nitrates and other impurities using centrifuge. The obtained samples were calcined at 400 °C for about 4 h and labeled as MnC-H.

Characterization

The crystal structure of the as-synthesized powder was identified using Bruker D2 Phaser powder X-ray diffractometer using CuK_α radiation ($\lambda = 1.5418$ Å) in the range of 10°–80° with step mode of 0.02° min^{-1}. Spinel formation of the compound and presence of functional groups were analyzed by FT-IR spectrophotometer (BRUKER ALPHA) using opus 6.5 (version) software. IR measurements were carried out at room temperature in the range from 500 to 4000 cm^{-1}. X-ray photoelectron spectroscopy (XPS) measurement was conducted by Kratos analytical axis Ultra DLD using monochromatized Al Kα1 source. The energy of an X-ray photon of 1.486 keV with pass energy of 160 eV was used for the survey spectrum and 40 eV for narrow scans. CasaXPS software was used for peak fitting, and the procedure used for this analysis was kept consistent for all of the sample conditions. The surface morphology was analyzed using scanning electron microscopy (SEM) ULTRA 55 (Carl Zeiss, Germany). Electrochemical measurements such as cyclic voltammetry (CV), chronopotentiometry (CP), and electrochemical impedance spectroscopy (EIS) were carried out from electrochemical work station CHI 661 C using 3-compartment cell employing prepared working electrode, platinum wire as counter electrode and standard calomel electrode (SCE) as a reference electrode. These electrodes were then soaked into 1 M KOH electrolyte solution for electrochemical measurements. The mass of the electrode material was measured using Shimadzu AUX220 analytical balance of accuracy 0.01 mg.

Fabrication of working electrode and electrolyte for electrochemical characterization

The typical procedure of working electrode fabrication has been reported previously [20]. Adopting a similar procedure, the working electrode was fabricated using the following steps; 80 wt% of prepared $MnCo_2O_4$, 10 wt% activated carbon, and 10 wt% polyvinylidene fluoride were well mixed using an agate mortar until a homogeneous black powder was obtained. Then a few drop of 1-methyl-2-pyrrolidinone was added to the above mixture to make into a paste. This paste was coated onto nickel foil current collector in the size of 1×1 cm^2 with 0.5 mm thickness. After coating, the foil was dried in air atmosphere at room temperature. Then the foil was heat treated at 80 °C for 4 h. The mass of the active electrode material lies in the range of ∼0.2–0.4 mg.

Results and discussion

XRD studies

The phase purity and formation of the synthesized samples were determined by powder X-ray diffractometer (PXRD). Typical XRD patterns of nanocrystalline $MnCo_2O_4$ samples are shown in Fig. 1a. PXRD patterns display peaks corresponding to (111), (220), (311), (400), (422), (511), and (440) planes, which can be ascribed to the formation of spinel compound. XRD patterns are well matched to fcc spinel $MnCo_2O_4$ with fd3 m space group (standard JCPDS card No. 023-1237). XRD pattern of samples prepared by both methods were identical to one another. Absence of peaks other than those attributed to $MnCo_2O_4$ depicts the structural and phase purity of the prepared compounds. Hydrothermally prepared sample shows better crystallinity than combustion-prepared $MnCo_2O_4$. A peak broadening was observed for the (311) plane of MnC-H. Generally, a peak broadening is associated with decrease in crystallite size and stress/strains induced in the nanoparticles. The average crystallite size (d) was calculated from the Scherrer formula [35],

Fig. 1 a X-ray diffraction pattern and **b** FT-IR spectra of MnCo$_2$O$_4$ nanoparticles synthesized by combustion and hydrothermal route
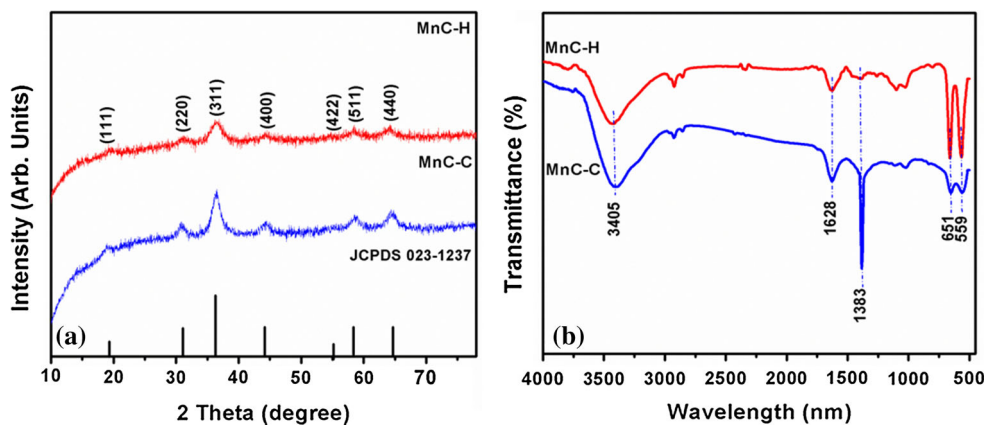
$$d = 0.9\,\lambda/(\beta\cos\theta), \quad (1)$$

where λ is the X-ray wavelength, β is the full-width at half maximum (FWHM), and θ is the diffraction angle. The average crystallite size of 24 nm was estimated for MnC-H and 26 nm for MnC-C samples.

FT-IR studies

Fourier transform infrared spectroscopy (FT-IR) was employed to identify the functional groups attached to MnCo$_2$O$_4$ nanoparticles. Figure 1b displays the FT-IR spectra of synthesized MnCo$_2$O$_4$ nanoparticles by combustion and hydrothermal route. In the spectra of MnCo$_2$O$_4$ nanoparticles, the broad band absorption at 3405 cm^{-1} corresponded to the O–H stretching vibration of physic-adsorbed water [36]. The peak from angular deformation of absorbed water molecules appeared at 1628 cm^{-1}. The peak at 1383 cm^{-1} can be assigned to the vibrational stretching of the C–N group, originated from the residual nitrate ions or glycine (fuel) present in the compound [37]. Two strong absorption bands at 651 and 559 cm^{-1} was observed in the FT-IR spectrum of both the samples, characteristic to spinel MnCo$_2$O$_4$ compounds [38]. These bands mainly correspond to the vibrational modes of metal–oxygen by the tetrahedrally bonded Mn^{2+} and octahedrally coordinated Co^{2+} ions, respectively [39]. This FT-IR absorption data confirm the successful formation of phase pure spinel MnCo$_2$O$_4$ in agreement with the XRD studies.

X-ray photoelectron spectroscopy studies

Elemental composition and chemical state of the compound was analyzed using XPS study and the results are presented in Figs. 2 and 3. Various elements present in the compound are displayed in the survey spectrum of the samples shown in Fig. 2a, b. For obtaining much

information on the chemical state of cobalt and manganese ions Co 2p and Mn 2p, high-resolution spectra were analyzed, as shown in Fig. 3.

Co 2p peak is split into two major peaks corresponding to Co 2p$_{1/2}$ and Co 2p$_{3/2}$ with spin orbital splitting energy of ~15 eV. Additionally, two shake-up satellite peaks were observed in the Co 2p spectra typical for spinel cobaltites. Details of peak position and spin orbital splitting energy are provided in the Table 1. Generally, Co 2p$_{3/2}$ peak at 779.07–779.67 eV and a spin orbit splitting energy of 15.2 eV are characteristics of Co^{3+} ions [40]. Appearance of first satellite peak at 783.75 eV with a difference of 3.5–6.5 eV above the Co 2p$_{3/2}$ peak is the characteristics of Co^{2+} ions, and second satellite peak at 803.65 eV with a difference of 9–10 eV above the Co 2p$_{1/2}$ main peak is characteristic of Co^{3+} ions. This confirms the presence of two types of Co ions in the compound. Co^{2+}/Co^{3+} ratio of MnCo$_2$O$_4$ prepared by combustion method is higher compared to MnC-H.

To determine manganese oxidation state, Mn 2p spectra and Mn 3s spectra were used. It is seen from the Fig. 3c, d. Mn 2p peak is split into two peaks corresponding to Mn 2p$_{1/2}$ and Mn 2p$_{3/2}$ with spin orbital splitting energy of ~11.5 eV. Mn 2p$_{3/2}$ peak at 641.1–641.6 eV binding energy and spin orbital splitting energy (Mn 2p$_{1/2}$–Mn 2p$_{3/2}$) of ~11.5 eV are associated with Mn^{3+} ions [41]. This result is in good agreement with the literatures reporting predominant tendency of Mn^{3+} ions to occupy octahedral site in spinel cobaltites. The spin orbit splitting energy of Mn 3s is associated with the mean oxidation state of manganese ions present in the compound. Mn 3s spin orbit splitting energy of the samples was calculated to be around 5.2 eV, which corresponds to Mn^{3+} ions in the compound [42].

O 1s high-resolution spectrum recorded for the samples is shown in Fig. 2c, d. On deconvoluting, the O 1s peak possess three component peaks, one about 529 eV corresponds to metal oxygen bond (M–O, M–Co, Mn), second
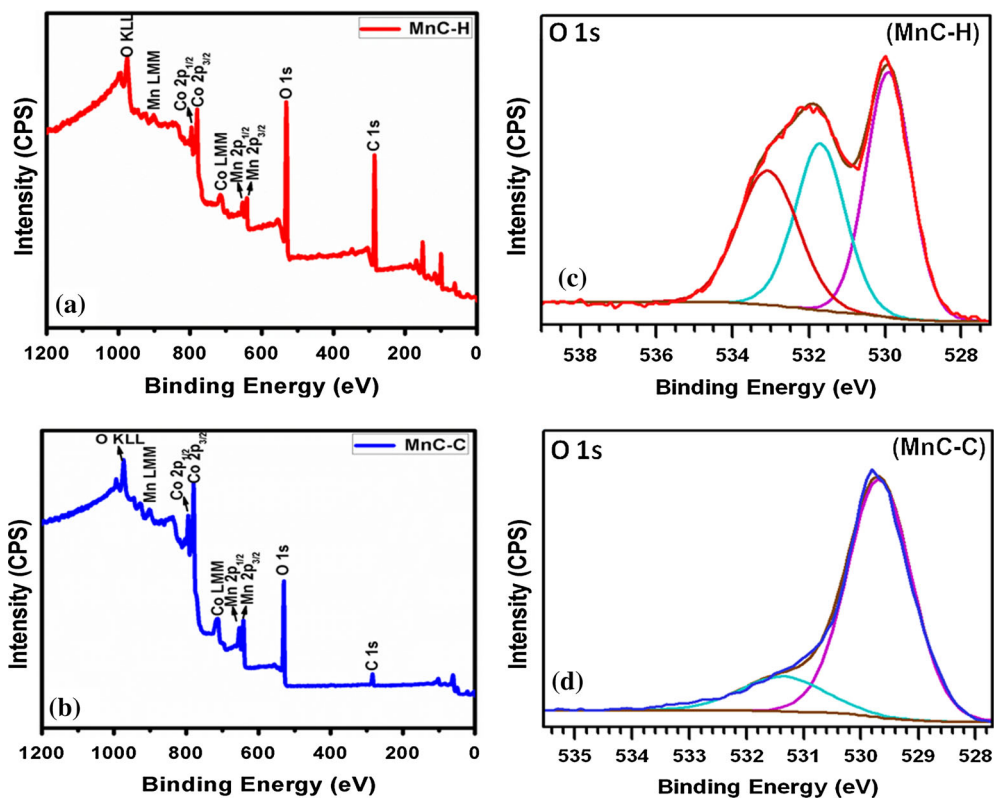
Fig. 2 Wide XPS spectrum and O 1s of MnCo$_2$O$_4$ nanoparticles by hydrothermal route (**a**, **c**) and combustion (**b**, **d**)

Fig. 3 XPS spectra of Mn 2p and Co 2p peak for MnCo$_2$O$_4$ nanoparticles by hydrothermal (**a**, **c**) and combustion route (**b**, **d**)
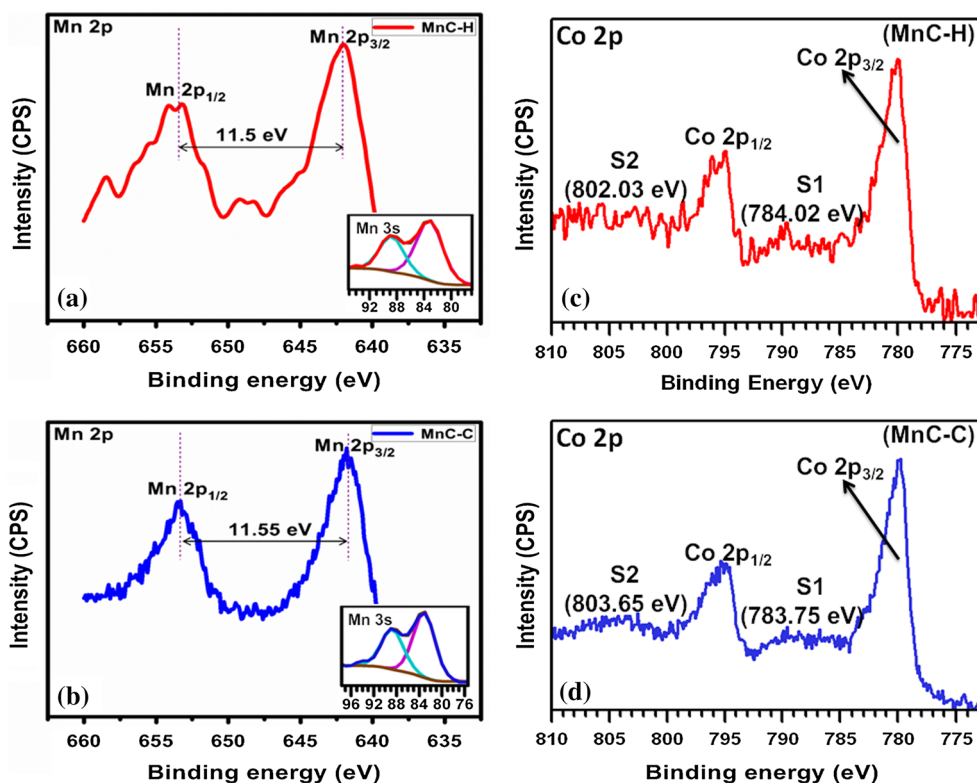
Table 1 Quantitative analysis of Co 2p, Mn 2p and Mn 3s spectra

Samples	Co 2p					Mn 2p			Mn 3s		
	Co $2p_{1/2}$	Co $2p_{3/2}$	Δ^a	S1	S2	Mn $2p_{1/2}$	Mn $2p_{3/2}$	Δ^b	Peak1	Peak2	Δ^c
MnC-C	794.71	779.52	15.19	783.75	803.65	653.36	641.81	11.55	87.85	82.72	5.13
MnC-H	794.70	779.50	15.20	784.02	802.03	652.84	641.34	11.5	88.23	83.05	5.18

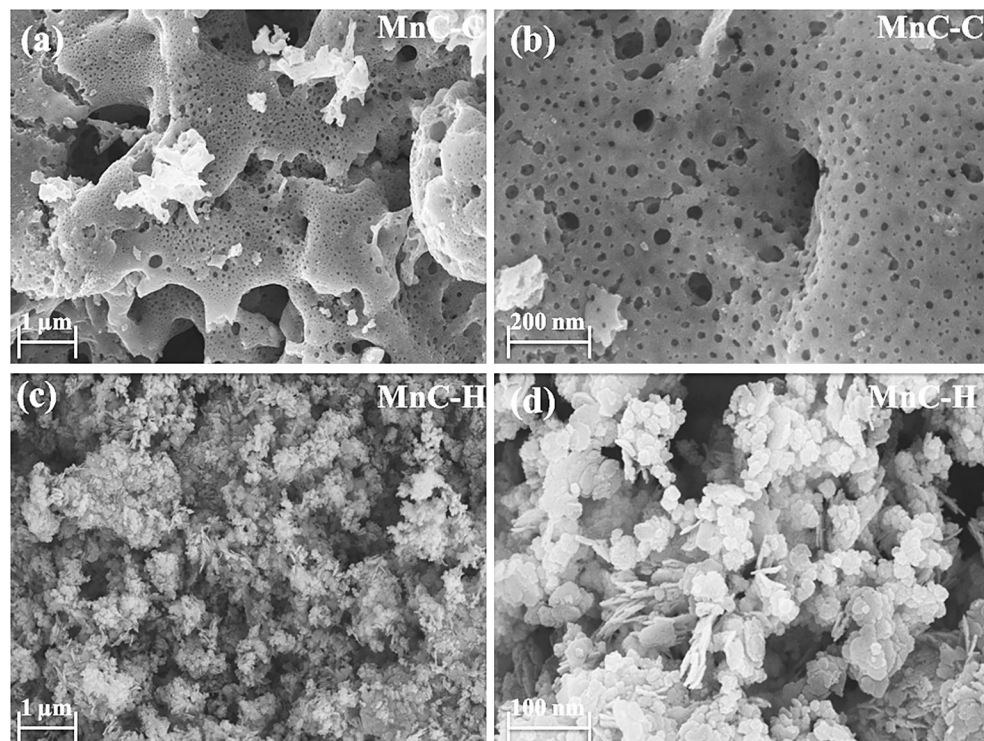[a,b,c] Spin orbit splitting for Co 2p, Mn 2p and Mn 3s, S1 and S2—satellite peaks of Co 2p

Fig. 4 SEM images of MnCo$_2$O$_4$ nanoparticles (**a**, **b**) combustion and (**c**, **d**) hydrothermal route

peak at 531 eV is a typical of oxygen in an OH group and strongly supports the presence of a hydroxyl species such as CoOOH and MnOOH, and third at 532 eV corresponds to surface bonded water (H–O–H). Narrow O 1s spectrum of combustion-prepared sample reveals that majority of the oxygen species is bonded to the metal ions. Hydrothermally prepared MnCo$_2$O$_4$ contains higher concentration of OH groups compared to combustion prepared which is in good agreement with the FT-IR results.

Morphology studies

In order to understand the changes occurring in morphology and particle size of the MnCo$_2$O$_4$ with growth mechanisms, the scanning electron microscope (SEM) analysis were performed. Figure 4a–d shows the typical

microstructures of spinel MnCo$_2$O$_4$ prepared by combustion and hydrothermal routes. Nanoparticles prepared by combustion method exhibits an agglomerated spongy network structure with voids or pores. Large volumes of gases released during the combustion process at critical temperatures have created numerous pores in the sample morphology. High magnification image (Fig. 4b) depicts the porous morphology of the material composed of pores of size ranging from nanoporous to macroporous regime. Further, SEM photographs of nanoparticles synthesized by hydrothermal method (Fig. 4c, d) shows loosely packed agglomerates consisting of interconnected nanoparticles exhibiting a flake-like spherical structures. This kind of morphology may lead to an increase in the surface area of the electrode materials thereby increasing the wetting ability of the electrode materials which plays a vital role in

electrochemical processes. Such surface structures facilitate mass transfer (i.e., electrolyte penetration and ion transport) and enhance electrolyte-accessible areas [43]. Thus, from the information obtained by SEM, we can conclude that the hydrothermally prepared nanoparticles could be favorable for supercapacitor applications.

Surface area measurements

To further analyze the structure of prepared samples, the nitrogen adsorption–desorption isotherms were measured. Figure 5 shows adsorption–desorption isotherms of samples, and the pore size distribution curves obtained from the desorption branch. The isotherm of MnC-C and MnC-H can be categorized as type IV according to the IUPAC classification with a distinct hysteresis loop. Appearance of hysteresis between $P/P_0 = 0.4$ to 1 in the isotherms indicates the mesoporous nature of the prepared compounds [44]. Steep increase in the absorption at $P/P_0 > 0.9$ suggests the contribution of macropores to the total surface area of the samples [45]. The BET surface areas, calculated from adsorption isotherms, show that the surface area of the MnC-C and MnC-H were 19.25 and 47.15 m^2g^{-1} respectively. High surface area of MnC-H indicates the higher interfacial area between the electrode and electrolyte. Pore size distribution curves provided alongside of the isotherm denotes the narrow distribution of pores in the prepared samples. In MnC-C majority of pores were found

lying in the micropore region centering at 1.85 nm. While in the case of MnC-H majority of pores size ranges between 2 and 6 nm centering at 3.77 nm falling within the optimal pore size range of 2–5 nm for supercapacitor applications [46]. Average pore radius estimated from BJH method for MnC-C and MnC-H is 11.78 and 14.5 nm respectively. Details of the surface area measurement are tabulated in Table 2. BET results validate the predictions made from SEM images. From the surface area measurements, it is speculated that $MnCo_2O_4$ prepared by hydrothermal method will show better electrochemical performance than combustion-prepared sample.

Electrochemical performance

Cyclic voltammetry (CV) studies

To examine the capacitive behavior of the prepared electrode material, CV technique was used. Figure 6a shows the CV curve recorded at 5 mV s^{-1} scan rate. $MnCo_2O_4$ prepared by both methods exhibits pair of typical redox peaks depicting the major type of charge storage in the material as faradaic consistent with the earlier reports by Kong et al. [43] and Zhang et al. [47]. Between, −0.1 and 0.2 V potential region, CV curves of both electrode materials resemble nearly rectangular shape characteristic of ideal capacitance. Couple of redox peaks observed was originated from the reversible transition between the

Fig. 5 N$_2$ adsorption–desorption measurements of MnCo$_2$O$_4$ nanoparticles (**a**, **c**) combustion and (**b**, **d**) hydrothermal route
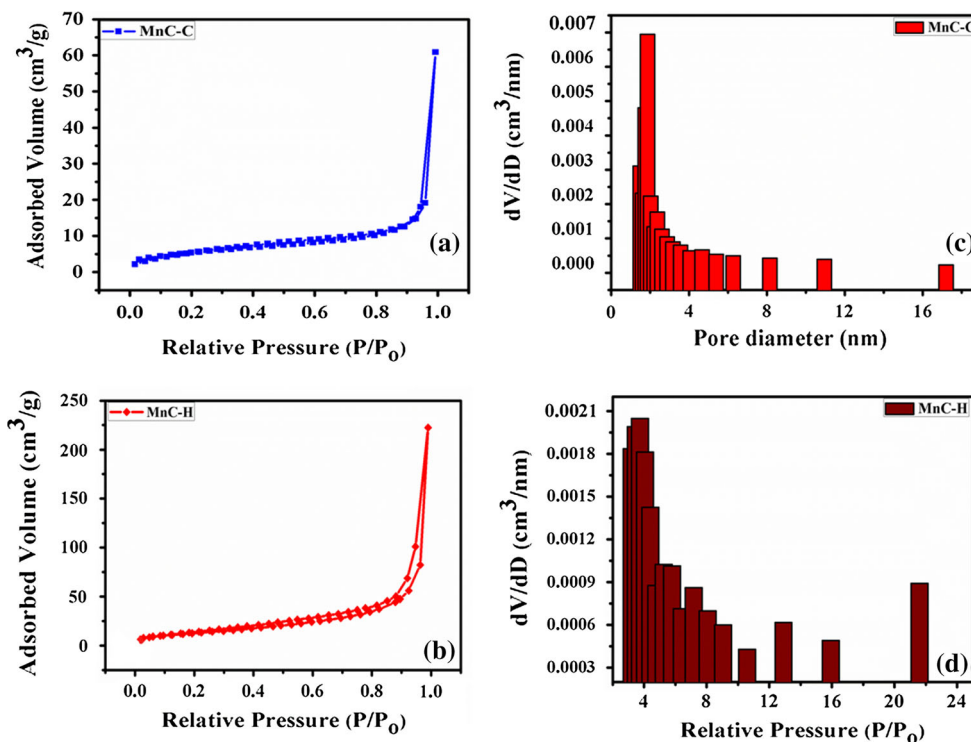
Table 2 Surface properties of the samples obtained from N_2 adsorption–desorption measurement
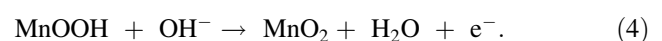
Sample name	BET surface area ($m^2\ g^{-1}$)	Average pore radius (nm)	Average pore volume ($cm^3\ g^{-1}$)	Specific capacitance ($F\ g^{-1}$)
MnC-C	19.25	11.78	0.1060	510
MnC-H	47.15	14.59	0.1498	671

Fig. 6 a Cyclic voltammograms of the electrodes recorded at 5 mVs^{-1}, **b** shows the charge–discharge curve of MnC-C and MnC-H at 0.5 A g^{-1}, **c** and **d** displays the CV curves recorded between the scan rate of 5–100 mV s^{-1} in 1 M KOH aqueous electrolyte for MnCo$_2$O$_4$ nanoparticles prepared by hydrothermal and combustion, respectively
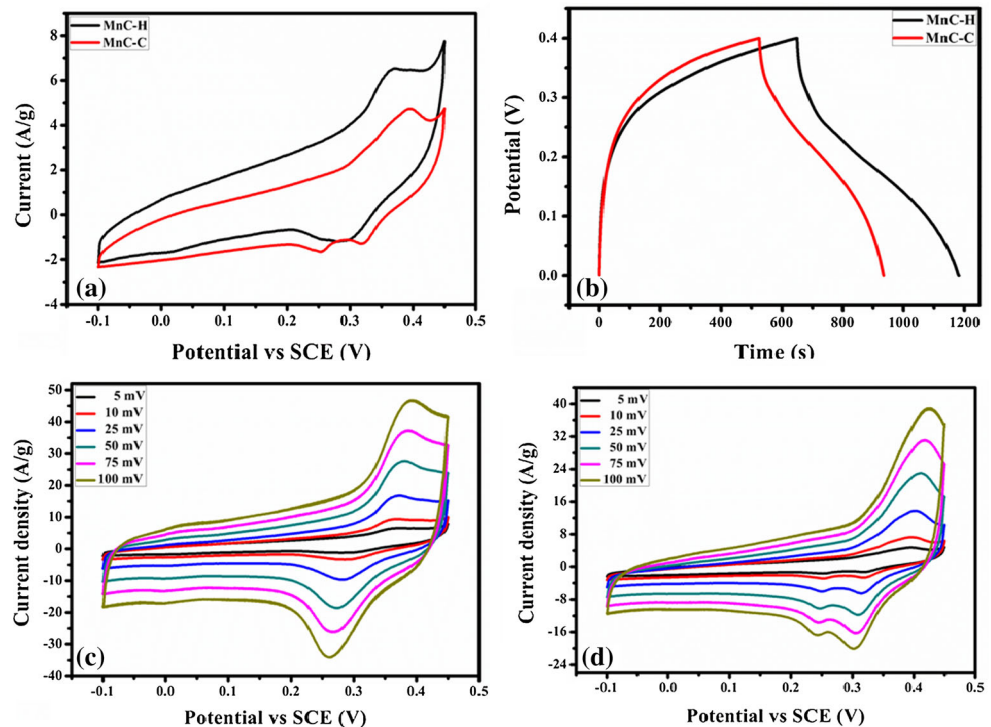
oxidation states of cobalt (Co^{2+} and Co^{3+}) and manganese ions (Mn^{3+}). In the place of large cathodic peak observed in the CV curve of MnC-H, a pair of reduction peaks appeared for MnC-C. This dissimilar nature of the redox peaks, while the oxidation and reduction potentials remain the same for Co^{2+}/Co^{3+} and Mn^{3+} species indicates the different electro-activeness of $MnCo_2O_4$ synthesized by two different conditions. It is very difficult to identify peaks corresponding to cobalt and manganese ions separately in the CV curve as they were identical in their reactivity. Capacitance of the material is largely influenced by the crystallinity, pore size, surface area, and chemical composition of the material. In our case, two different types of electrochemical performance can be attributed to the difference in Co^{2+}/Co^{3+} ratio between MnC-H and MnC-C determined from the XPS studies. Appearance of cathodic doublet peak in the CV curve of MnC-C is attributed to the higher Co^{3+} and Mn^{3+} ions concentration in the prepared samples, similar results have been reported previously [28]. In the case of MnC-H, the transitions are highly accelerated such that pair of redox peaks convolutes

to form a single peak. Area under the curve indicates the volume of SC exhibited by the material. Clearly, MnC-H portrays large area under the CV curve. Under controlled hydrothermal synthesis condition, $MnCo_2O_4$ particle forms into loosely packed flake-like spherical particle that increases the interfacial area and simultaneously facilitates facile insertion/exertion of electrolyte ions between the layers. Whereas, aggregates of nanoparticles forming foam-like structure is less beneficial in terms of electrolyte accessibility. Electrochemical reaction responsible for the large current response is given below [21],

$$MnCo_2O_4 + H_2O + OH^- \rightarrow 2CoOOH + MnOOH + e^-$$

$$(2)$$

$$CoOOH + OH^- \leftrightarrow CoO_2 + H_2O + e^- \qquad (3)$$

$$MnOOH + OH^- \rightarrow MnO_2 + H_2O + e^-. \qquad (4)$$
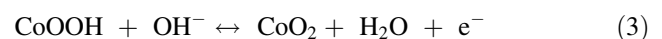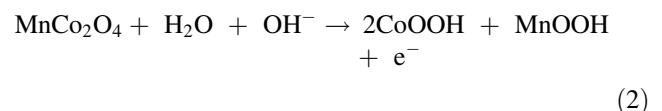
These transitions were highly fast and reversible. High-rate performance of the MnC-H and MnC-C electrode material was tested by sweeping the electrode material at

high scan rates and the results were presented in Fig. 6c, d, respectively. Negligible shift in the peaks with increase in scan rate depicts the low polarization resistance of MnC-H electrode, while considerable shift was observed in the CV curves of MnC-C. High BET surface area of the hydrothermally prepared nanoparticle is beneficial for the facile transport of electrolyte ions into the electrode material. SC of the material can be calculated from the area under the curve using below equation [48],

$$SC = [1/V \times m(Va - Vc)] * \int_{Va}^{Vc} IV \, dV \qquad (5)$$

The SC values were calculated graphically by integrating the area under the I–V curves and then dividing by the sweep rate (V s^{-1}), the mass of the material (m), and the potential window (Va to Vc). Maximum SC of 671 F g^{-1} calculated for MnC-H at 5 mV s^{-1} was relatively higher than the SC calculated for MnC-C (510 F g^{-1}). The reported values are higher than Mn–Co oxide/PEDOT electrodes with rod-like structures prepared by Babakhani and Ivey (310 F g^{-1}) [6] and one-dimension MnCo$_2$O$_4$ nanowire arrays on nickel foam synthesized using facile hydrothermal method by Li et al. (349.8 F g^{-1}) [14]. High capacitance of the prepared compounds can be attributed to the nanoporous nature of the electrodes. As expected from BET studies, MnC-H shows better electrochemical performance than combustion-prepared (MnC-C) electrode material.

Chronopotentiometric studies

Charge–discharge profile of the material was examined using CP technique. Figure 6b shows the charge/discharge profile of the samples crystallized by two different methods at a current density of 0.5 A g^{-1}. Potential non-linear-dependent current responses reveal the faradaic nature of the material, which is in good agreement with the CV results. CP curve recorded at higher current densities is shown in Fig. 7a, b. SC can be calculated from galvanostatic study using the below equation:

$$SC = I * t_d/m * \Delta V, \qquad (6)$$

where I is the constant current applied, t_d is the discharge time, m is the mass of the material loaded, and ΔV is the potential difference. Calculated SC values were almost similar to those obtained from the CV study. Cycling life of the material was also tested by performing continuous charge–discharge at 3 A g^{-1} current density for 1000 cycles. 92 % of the initial capacitance was retained by MnC-H after 1000 cycles, whereas only 84 % of the capacitance was retained by MnC-C material (Fig. 7c). Higher concentration of micropores present in MnC-C, as determined from the surface area analysis, retards the mass transfer during the charge–discharge process [46].

Fig. 7 Charge–discharge recorded between the scan rate of 0.5–10 A g^{-1} (a, b), specific capacitance as a function of cycle number recorded at a current density of 3 A g^{-1} (insert long 1000 cycling studies) (c), impedance spectra (Nyquist plot) recorded between 1 Hz and 100 kHz (inset of the figure shows the enlarged portion of the curve at high frequency region) (d) for MnCo$_2$O$_4$ nanoparticles by combustion and hydrothermal route
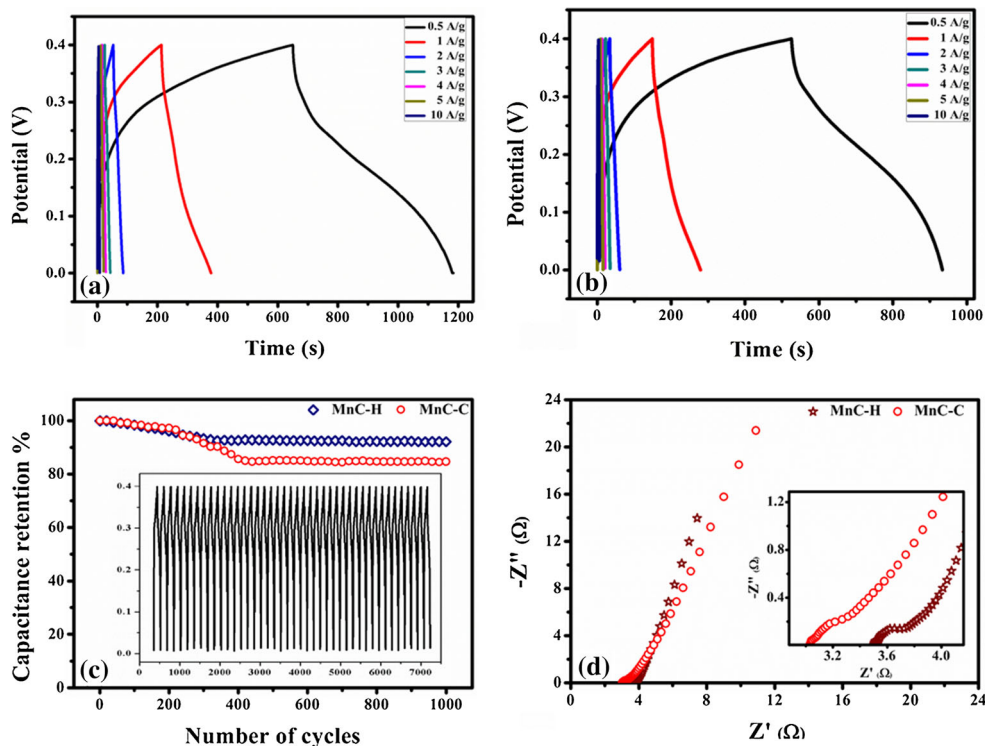
Electrochemical impedance studies

EIS was employed to investigate the rate kinetics and charge transport during electrochemical reactions. Figure 7d shows the impedance spectra (Nyquist plot) recorded between 1 Hz and 100 kHz. Inset of the figure shows the enlarged portion of the curve at high frequency region. Semi-circle observed in both spectra depicts the charge transfer resistance in the material. Intercept of curve on the real part of the Nyquist plot gives the measure of equivalent series resistance (ESR) or solution resistance. Surprisingly, $MnCo_2O_4$ prepared by combustion method shows low ESR value of 3.02 Ω compared to 3.51 Ω observed for MnC-H. Slope of the line in the low frequency region gives the measure of Warburg impedance or diffusion resistance. Linear line almost parallel to the y-axis denotes lower diffusion resistance offered by MnC-H. Lower diffusion resistance can be attributed to the flake-like morphology that favors better transport of electrolyte ions. From the overall electrochemical results, $MnCo_2O_4$ prepared by hydrothermal method shows superior performance than $MnCo_2O_4$ prepared by combustion method.

Conclusions

Manganese cobaltite nanoparticles were prepared by two different synthesis conditions and characterized thoroughly. Phase purity and spinel formation of the compound were determined from XRD and FT-IR studies. Chemical composition and elemental analysis were performed using XPS technique. Mixed oxidation state of cobalt ions (Co^{2+} and Co^{3+}) and Mn^{3+} oxidation state of manganese typical for an inverse $MnCo_2O_4$ spinel compound were determined. FESEM images reveal the flake-like and sponge-like morphologies of MnC-H and MnC-C, respectively. Nanoporous characteristics of the prepared samples were determined from BET measurements. Pseudocapacitive behavior of the materials was evident from CV and CP studies. Influence of morphology and chemical state of the material on the electrochemical performance of the electrode materials was recognized from the capacitive studies. EIS spectra reveal the lower diffusion resistance offered by hydrothermally prepared $MnCo_2O_4$ owing to its unique flake-like morphology. From the overall electrochemical performances, $MnCo_2O_4$ prepared by controlled synthesis method shows better capacitive performance and proves to be a promising material for supercapacitor applications.

References

1. Yang L, Cheng S, Ding Y, Zhu X, Wang ZL, Liu M (2012) Hierarchical network architectures of carbon fiber paper supported cobalt oxide nanonet for high-capacity pseudocapacitors. Nano Lett 12:321–325. doi:10.1021/nl203600x
2. Zhou W, Liu J, Chen Tao, Tan KS, Jia X, Luo Z, Cong C, Yang H, Li CM, Ting Y (2011) Fabrication of Co_3O_4-reduced graphene oxide scrolls for high-performance supercapacitor electrodes. Phys Chem Chem Phys 13:14462–14465. doi:10.1039/c1cp21917k
3. Djurfors B, Broughton JN, Brett MJ, Ivey DG (2003) Microstructural characterization of porous manganese thin films for electrochemical supercapacitor applications. J Mater Sci 38:4817–4830. doi:10.1023/B:JMSC.0000004401.81145.b6
4. Deng J-J, Deng J-C, Liu Z-L, Deng H-R, Liu B (2009) Influence of addition of cobalt oxide on microstructure and electrochemical capacitive performance of nickel oxide. J Solid State Electrochem 13:1387–1394. doi:10.1007/s10008-008-0701-5
5. Chang J-K, Hsieh W-C, Tsai W-T (2008) Effects of the Co content in the material characteristics and supercapacitive performance of binary Mn–Co oxide electrodes. J Alloys Compd 461:667–674. doi:10.1016/j.jallcom.2007.07.092
6. Babakhani B, Ivey DG (2011) Investigation of electrochemical behavior of Mn–Co doped oxide electrodes for electrochemical capacitors. Electrochim Acta 56:4753–4762. doi:10.1016/j.electacta.2011.03.008
7. Wu H-Y, Wang H-W (2012) Electrochemical synthesis of nickel oxide nanoparticulate films on nickel foils for high-performance electrode materials of supercapacitors. Int J Electrochem Sci 7:4405–4417
8. Wang D, Li Y, Wang Q, Wang T (2012) Nanostructured Fe_2O_3–graphene composite as a novel electrode material for supercapacitors. J Solid State Electrochem 16:2095–2102. doi:10.1007/s10008-011-1620-4
9. Hinklin TR, Azurdia J, Kim M, Marchal JC, Kumar S, Laine RM (2008) Finding spinel in all the wrong places. Adv Mater 20:1373–1375. doi:10.1002/adma.200702124
10. Yoon T-J, Kim JS, Kim BG, Yu KN, Cho M-H, Lee J-K (2005) Multifunctional nanoparticles possessing a magnetic motor effect for drug or gene delivery. Angew Chem Int Ed 44:1068–1071. doi:10.1002/anie.200461910
11. Marco JF, Gancedo RJ, Gracia M, Gautier JL, Rıos EI, Palmer HM, Greaves C, Berry FJ (2001) Cation distribution and magnetic structure of the ferrimagnetic spinel $NiCo_2O_4$. J Mater Chem 11:3087–3093. doi:10.1039/b103135j
12. Martin de Vidales JL, Garcia-Chain P, Rojas R, Vila E, Garcia-Martinez O (1998) Preparation and characterization of spinel-type Mn–Ni–Co–O negative temperature coefficient ceramic thermistors. J Mater Sci 33:1491–1496. doi:10.1023/A:1004351809932
13. Yokoyama T, Meguro T, Shimada Y, Tatami J, Komeya K, Abe Y (2007) Preparation and electrical properties of sintered oxides composed of $Mn_{1.5}Co_{(0.25+x)}Ni_{(1.25-x)}O_4$ with a cubic spinel structure. J Mater Sci 42:5860–5866. doi:10.1007/s10853-006-1141-1
14. Li L, Zhang YQ, Liu XY, Shi SJ, Zhao XY, Zhang H, Ge X, Cai GF, Gu CD, Wang XL, Tu JP (2014) One-dimension $MnCo_2O_4$ nanowire arrays for electrochemical energy storage. Electrochim Acta 116:467–474. doi:10.1016/j.electacta.2013.11.081
15. Gomez J, Kalu EE (2013) High-performance binder-free Co–Mn composite oxide supercapacitor electrode. J Power Sources 230:218–224. doi:10.1016/j.jpowsour.2012.12.069
16. Kim SW, Lee HW, Muralidharan P, Seo DH, Yoon WS, Kim D, Kang K (2011) Electrochemical performance and exsitu analysis

of ZnMn$_2$O$_4$ nanowires as anode materials for lithium rechargeable batteries. Nano Res 4:505–510. doi:10.1007/s12274-011-0106-0

17. Jiang H, Ma J, Li CZ (2012) Hierarchical porous NiCo$_2$O$_4$ nanowires for high-rate supercapacitors. Chem Commun 48:4465–4467. doi:10.1039/C2CC31418E

18. Wang Z, Zhang X, Li Y, Liu ZT, Hao ZP (2013) Synthesis of graphene–NiFe$_2$O$_4$ nanocomposites and their electrochemical capacitive behavior. J Mater Chem A 1:6393–6399. doi:10.1039/C3TA10433H

19. Karthikeyan K, Kalpana D, Renganathan NG (2009) Synthesis and characterizationof ZnCo$_2$O$_4$ nanomaterial for symmetric supercapacitor applications. Ionics 15:107–110. doi:10.1007/s11581-008-0227-y

20. Naveen AN, Selladurai S (2014) Investigation on physiochemical properties of Mn substituted spinel cobalt oxide for supercapacitor applications. Electrochim Acta 125:404–414. doi:10.1016/j.electacta.2014.01.161

21. Prasad KR, Miura N (2004) Electrochemically synthesized MnO$_2$-based mixed oxides for high performance redox supercapacitors. Electrochem Commun 6:1004–1008. doi:10.1016/j.elecom.2004.07.017

22. Bordeneuve H, Tenailleau C, Guillemet-Fritsch S, Smith R, Suard E, Rousset A (2010) Structural variations and cation distributions in Mn$_{3-x}$Co$_x$O$_4$ (0 < x < 3) dense ceramics using neutron diffraction data. Solid State Sci 12:379–386. doi:10.1016/j.solidstatesciences.2009.11.018

23. Gautier JL, Rios E, Gracia M, Marco JF, Gancedo JR (1997) Characterisation by X-ray photoelectron spectroscopy of thin Mn$_x$Co$_{3-x}$O$_4$ (1 ≥ x ≥ 0) spinel films prepared by low-temperature spray pyrolysis. Thin Solid Films 311:51–57. doi:10.1016/S0040-6090(97)00463-X

24. Blasse G (1963) Superexchange in the spinel structure. Some magnetic properties of oxides M^{2+}Co$_2$O$_4$ and M^{2+}Rh$_2$O$_4$ with spinel structure. Philips Res Rep Suppl 18:383

25. Kolomiets BT, Sheftel J, Kurlina E (1957) Electrical properties of some compound oxide semiconductors. Sov Phys Tech Phys 2:40–58

26. Wickham DG, Croft W (1958) Crystallographic and magnetic properties of several spinels containing trivalent ja-1044 manganese. J Phys Chem Solids 7:351

27. Gubanov A (1957) Sov Phys I.C.S. Technol Phys 2:47

28. Sutka A, Mezinskis G (2012) Sol–gel auto-combustion synthesis of spinel-type ferrite nanomaterials. Front Mater Sci 6:128–141. doi:10.1007/s11706-012-0167-3

29. Verma S, Joshi HM, Jagadale T, Chawla A, Chandra R, Ogale S (2008) Nearly monodispersed multifunctional NiCo$_2$O$_4$ spinel nanoparticles: magnetism, infrared transparency and radiofrequency absorption. J Phys Chem C 112:15106–15112. doi:10.1021/jp804923t

30. Hayashi H, Hakuta Y (2010) Hydrothermal synthesis of metal oxide nanoparticles in supercritical water. Materials 3:3794–3817. doi:10.3390/ma3073794

31. Zhang X, Shi W, Zhu J, Zhao W, Ma J, Mhaisalkar S, Maria TL, Yang Y, Zhang H, Hng HH, Yan Q (2010) Synthesis of porous NiO nanocrystals with controllable surface area and their application as supercapacitor electrodes. Nano Res 3:643–652. doi:10.1007/s12274-010-0024-6

32. Meher SK, Rao GR (2011) Ultralayered Co$_3$O$_4$ for high-performance supercapacitor applications. J Phys Chem C 115:15646–15654. doi:10.1021/jp201200e

33. Du W, Liu R, Jiang Y, Lu Q, Fan Y, Gao F (2013) Facile synthesis of hollow Co$_3$O$_4$ boxes for high capacity supercapacitor. J Power Sources 227:101–105. doi:10.1016/j.jpowsour.2012.11.009

34. Duan BR, Cao Q (2012) Hierarchically porous Co$_3$O$_4$ film prepared by hydrothermal synthesis method based on colloidal crystal template for supercapacitor application. Electrochim Acta 64:154–161. doi:10.1016/j.electacta.2012.01.004

35. Tholkappiyan R, Vishista K (2014) Influence of lanthanum on the optomagnetic properties of zinc ferrite prepared by combustion method. Physica B 448:177–183. doi:10.1016/j.physb.2014.04.022

36. Subramanian V, Hall SC, Smith PH, Rambabu B (2004) Mesoporous anhydrous RuO$_2$ as a supercapacitor electrode material. Solid State Ionics 175:511–515. doi:10.1016/j.ssi.2004.01.070

37. Vu D, Li X, Li Z, Wang C (2013) Phase-structure effects of electrospun TiO$_2$ nanofiber membranes on As(III) adsorption. J Chem Eng Data 58:71–77. doi:10.1021/je301017q

38. Luo W, Hu X, Sun Y, Huang Y (2012) Electrospun porous ZnCo$_2$O$_4$ nanotubes as a high-performance anode material for lithium-ion batteries. J Mater Chem 22:8916–8921. doi:10.1039/c2jm00094f

39. Rojas RM, Vila E, García O, de Vidales JLM (1994) Thermal behaviour and reactivity of manganese cobaltites Mn$_x$Co$_{3-x}$O$_4$(0.0 ≤ x ≤ 1.0) obtained at low temperature. J Mater Chem 4:1635–1639. doi:10.1039/jm9940401635

40. Tan BJ, Klabunde KJ, Sherwood PMA (1991) XPS studies of solvated metal atom dispersed (SMAD) catalysts. Evidence for layered cobalt-manganese particles on alumina and silica. J Am Chem Soc 113:855–861. doi:10.1021/ja00003a019

41. Xia X-H, Tu J-P, Wang X-L, Gua C-D, Zhao X-B (2011) Mesoporous Co$_3$O$_4$ monolayer hollow-sphere array as electrochemical pseudocapacitor material. Chem Commun 47:5786–5788. doi:10.1039/C1CC11281C

42. Jiang H, Zhao T, Yan C, Ma J, Li C (2010) Hydrothermal synthesis of novel Mn$_3$O$_4$ nano-octahedrons with enhanced supercapacitors performances. Nanoscale 2:2195–2198. doi:10.1039/C0NR00257G

43. Kong L-B, Lu C, Liu M-C, Luo Y-C, Kang L, Li X, Walsh FC (2014) The specific capacitance of sol–gel synthesised spinel MnCo$_2$O$_4$ in analkaline electrolyte. Electrochim Acta 115:22–27. doi:10.1016/j.electacta.2013.10.089

44. Ding R, Qi L, Wang H (2012) A facile and cost-effective synthesis of mesoporous NiCo$_2$O$_4$ nanoparticles and their capacitive behavior in electrochemical capacitors. J Solid State Electrochem 16:3621–3633. doi:10.1007/s10008-012-1798-0

45. Meher SK, Rao GR (2011) Effect of microwave on the nanowire morphology, optical, magnetic, and pseudocapacitance behavior of Co$_3$O$_4$. J Phys Chem C 115:25543–25556. doi:10.1021/jp209165v

46. Wei T-Y, Chen C-H, Chang K-H, Lu S-Y, Hu C-C (2009) Cobalt oxide aerogels of ideal supercapacitive properties prepared with an epoxide synthetic route. Chem Mater 21:3228–3233. doi:10.1021/cm9007365

47. Zhang Y, Luo L, Zhang Z, Ding Y, Liu S, Deng D, Zhao H, Chen Y (2014) Synthesis of MnCo$_2$O$_4$ nanofibers by electrospinning and calcination: application for a highly sensitive non-enzymatic glucose sensor. J Mater Chem B 2:529–535. doi:10.1039/C3TB21288B

48. Srinivasan V, Weidner JW (2002) Capacitance studies of cobalt oxide films formed via electrochemical precipitation. J Power Sources 108:15–20. doi:10.1016/S0378-7753(01)01012-6